J. Fluid Mech. (1984), *vol.* 147, *pp.* 431–447
Printed in Great Britain

On the flow in a channel induction furnace

By A. J. MESTEL
Department of Applied Mathematics and Theoretical Physics, University of Cambridge

(Received 31 January 1984)

The channel induction furnace is an electrically efficient device for the heating and stirring of liquid metals. In this paper an axisymmetric model for the channel flow is proposed, in which the fluid is confined to the inside of a torus. An exact solution for the magnetic field is found in terms of toroidal harmonic functions. Finite-difference methods are used to calculate the primary, cross-channel motions under the assumptions of a small skin depth, a constant eddy viscosity and no thermal dependence. Non-axisymmetric perturbations to the channel shape are considered and the perturbed field calculated. The secondary circulation along the channel is discussed.

1. Introduction

The use of alternating magnetic fields to heat and stir liquid metals is fairly widespread in the metallurgical industry. These devices fall broadly into two categories known as 'coreless' and 'channel' induction furnaces respectively. The coreless furnace is conceptually the simpler, consisting of a container full of liquid metal surrounded by a coil carrying alternating current. The induced electric currents drive strong circulatory flows in the melt, as illustrated in figure 1 (*a*). In a channel furnace the electrical efficiency of the system is increased by topologically linking the liquid metal with a ferromagnetic core. This is achieved by the attachment to the bottom of the liquid-metal bath of both ends of a channel, through which the fluid passes. The core is then linked with the channel, and energized by means of an induction coil. The induced currents flow along the channel and connect up inside the main body of the metal, as illustrated in figure 1 (*b*). The system may be thought of as an electrical transformer with a closed loop of liquid metal playing the part of the secondary coil.

The advantages of the channel furnace over the coreless furnace are twofold. First, the channelling of the magnetic field by the highly permeable core reduces the leakage flux and the corresponding losses of electrical energy in surrounding conductors. Secondly, the thermal insulation around the main body of the fluid may be much thicker, since the magnetic field does not need to penetrate it. Heat losses are therefore significantly lower. These savings must be weighed against the relatively frequent need to service the channel section of the furnace because of erosion or build-up of metallic oxide. The rest of the furnace is eroded much more slowly, however. Thus, provided that the channel section is constructed as a separate, renewable part, the furnace as a whole may enjoy a considerable lifetime.

The main disadvantage of the channel furnace relates to the character of the fluid flow it drives. The Lorentz forces do not vary greatly along the channel, and thus the primary flow occurs in a channel cross-section. For the successful functioning of the device, however, it is essential for heat to be convected from the channel region,

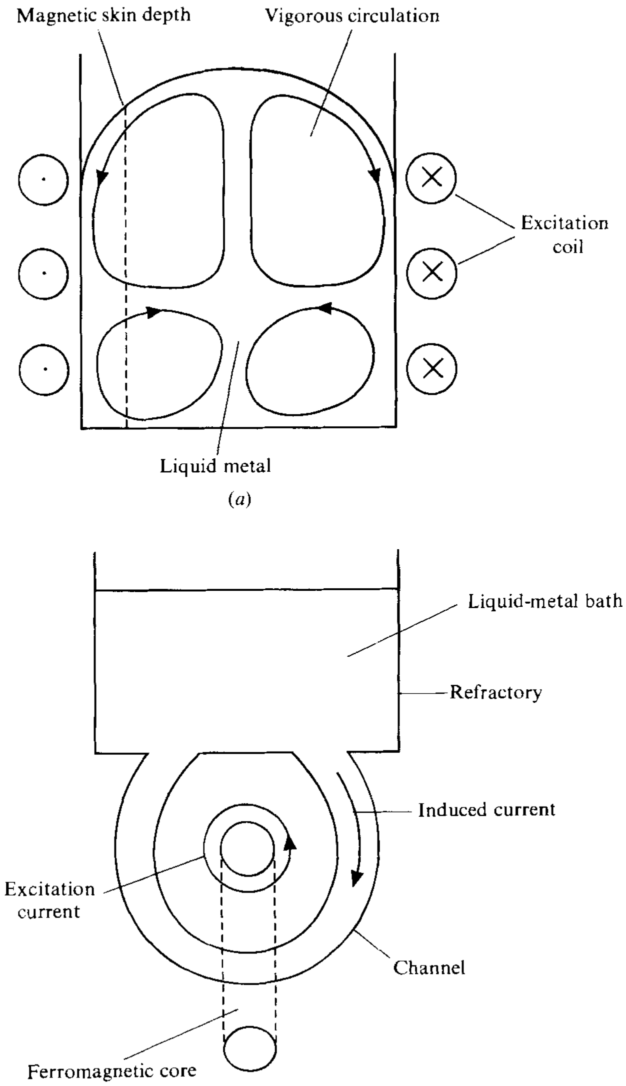

(a)

(b)

FIGURE 1 (*a*, *b*). For caption see facing page.

where it is generated, to the main body of the fluid in the bath. A secondary flow along the channel is thus required, which will entail circulation in the bath region. The relative weakness of this secondary motion renders the channel furnace less suitable for any process in which thorough mixing is required (e.g. in the production of alloys). The secondary flow can be quite complex, consisting of a superposition of a unidirectional drift and a system of irregular rolls spread along the channel (Schluckebier 1973).

In this paper our objective is to provide a quantitative model of the primary fluid motion across the channel, with the eventual aim of treating the secondary motions as perturbations on the primary flow. In §2 we formulate the mathematical model, and solve for the magnetic field in §3. In §4 we discuss the primary flow, which we then calculate in §§5 and 6. In §7 we consider the effect of non-axisymmetric perturbations, and conclude in §8.

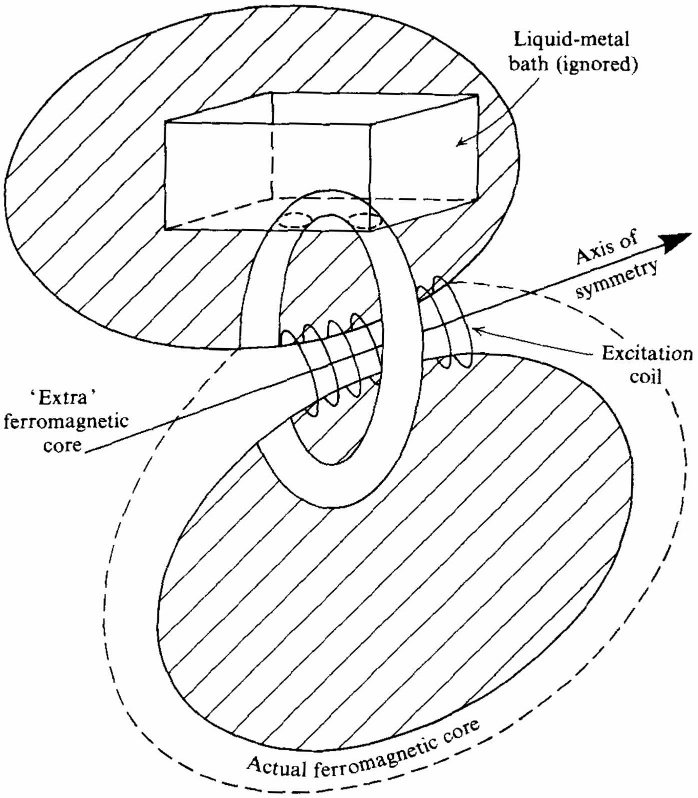

(*c*)

FIGURE 1. (*a*) The coreless induction furnace. (*b*) The channel induction furnace. (*c*) The axisymmetric model.

2. The mathematical model

The full equations for the magnetic field, fluid motions and heat transfer are, of course, difficult to solve, especially in a general geometry. An additional complication derives from the turbulence of the flow, which needs to be modelled. In this study we use the simple model whereby a constant 'eddy viscosity' ν is introduced to replace the kinematic molecular viscosity. We shall also neglect any effects of thermal variation, assuming that the rapid motions and high thermal conductivity ensure approximate uniformity of temperature in a channel cross-section. This assumption is certainly valid when calculating the primary cross-channel motion. It is less clear, though probably still true, that buoyancy-driven motions are small compared with those driven by the Lorentz force over the entire furnace.

The degree of penetration of the magnetic field into the metal is measured by the skin depth δ' defined by

$$\delta' = \left(\frac{1}{2\mu_0 \sigma \Omega}\right)^{\frac{1}{2}}, \tag{2.1}$$

where Ω is the field frequency, μ_0 the magnetic permeability and σ the electrical conductivity. For aluminium at 50 Hz this is about 3 cm, which we assume is small compared with the width of the channel. It is not absolutely necessary to make this assumption, but the extra work otherwise involved would be discommensurate with the increased accuracy thereby attained. Should δ' be so large that the field significantly penetrates the bath, however, then a situation may occur different to that considered here, in which the secondary motions are as great as the primary. This may happen if a secondary flow path develops which excludes a large region of vorticity generation (Alden, Burke & Biringer 1970). This phenomenon has been observed in model furnaces at mains frequency, and corresponds to a very low operational frequency for a real furnace, with a correspondingly low heat input. Under normal working conditions the skin depth is small, though not negligible.

The magnetic Reynolds number R_m, which measures the importance of advection of field lines by the fluid, is defined by

$$R_m = U_0 d \mu_0 \sigma, \tag{2.2}$$

where U_0 and d are a typical velocity scale and lengthscale respectively. As usual in liquid-metal MHD, we have $R_m \ll 1$, especially in the high-frequency case, when the effective magnetic Reynolds number is two orders of δ'/d smaller. This ensures that the magnetic field may be calculated as if the metal were in fact solid. The Lorentz force then follows by direct calculation, and will, in general, have both a steady part, and one oscillating with twice the driving frequency. Inertia prevents the fluid responding to variations in the driving force of such high frequency, and thus the motion we seek is that steady motion arising from the time-averaged part of the Lorentz force.

A full, three-dimensional model of the channel furnace would be difficult to construct, and expensive to solve in terms of computing time. Some aspects of the furnace can, however, be reproduced by means of an axisymmetric model, and the non-axisymmetric processes may then be regarded as perturbations on the underlying structure. Along the channel, the magnetic field does not vary very much, because it depends mainly on distance from the excitation coil, which is more or less constant along the side of the channel nearest the coil. The bottom of the bath may be regarded as a change in the cross-section of the channel, which we treat as small. The other variations from axisymmetry – the top of the bath, and the return path of the iron core – only affect the field in the regions where it is weaker, on the far side of the channel from the coil.

We shall consider a furnace whose channel has a circular cross-section, as the sharp corners associated with a rectangular channel lead to unnecessary complications. For similar reasons, we shall assume that the iron core has a circular shape, though we allow its size and position to vary relative to the channel.

In order to make the model axisymmetric, we must formalize two approximations to the geometry. First, we ignore the presence of the bath above the channel, and consider the metal to be confined to the interior of a rigid torus. This assumption removes the dynamical effects associated with the entrance and exit regions of the channel. While these are important in driving the secondary flows, they do not greatly influence the primary fluid motion, which occurs in a cross-section of the channel.

The second approximation concerns the return path of the iron core, which introduces a slight asymmetry into the set-up. The system could be made axisymmetric by moving the return path to infinity, but it is more general instead to consider the core as returning symmetrically about the axis of the (now toroidal) channel. Since we are assuming a circular shape for the iron core, we may regard the entire system as lying inside a toroidal hole in a ferromagnetic core. The excitation coil and the channel circle round inside this hole. The case where the return path is at infinity may be considered as a limit of this system as the dimensions of the tori corresponding to the channel and the core are varied. The axisymmetric model is illustrated in figure 1 (*c*).

The advantage of the chosen geometry is that it enables an exact mathematical solution for the magnetic field to be found. The surfaces of the channel and the core may be made into coordinate surfaces of a coordinate system in which Laplace's equation permits separable solutions. These toroidal coordinates are described in the Appendix.

3. The magnetic field

We represent the magnetic field by $\mathrm{Re}\,(\boldsymbol{B}\mathrm{e}^{\mathrm{i}\Omega t})$, where Re denotes the real part. Inside the metal channel, because of the smallness of the magnetic Reynolds number, $\boldsymbol{B}$ obeys a diffusion equation

$$\mathrm{i}\Omega\mu_0\sigma\boldsymbol{B} = \nabla^2\boldsymbol{B}. \tag{3.1}$$

Under the skin-depth approximation, tangential derivatives in the Laplacian are neglected in favour of the normal derivatives. In terms of toroidal coordinates (θ,μ,ϕ) we obtain the (solenoidal) solution

$$\boldsymbol{B} = \left[(1+\mathrm{i})B_{\mathrm{s}}(\theta),\ -\frac{2\delta'}{a}H^6\frac{\partial}{\partial\theta}\left(\frac{B_{\mathrm{s}}}{H^4}\right),\ 0\right]\mathrm{e}^{(1+\mathrm{i})\,n/2\delta'}, \tag{3.2}$$

where n is the normal distance from the surface, and

$$H = (\cosh\mu-\cos\theta)^{\frac{1}{2}} \tag{3.3}$$

is related to the scale factors for these coordinates. The function $B_{\mathrm{s}}(\theta)$ is determined by matching with the magnetic field outside the channel. It is, in fact, the tangential field that would occur were the metal a perfect conductor. To leading order in the skin depth, therefore, the correct boundary condition to be applied to the external field on the channel is one of zero normal field. Now the ferromagnetic core typically has a relative permeability of several thousand, and a finite tangential field outside it would give rise to a very large internal field. The boundary condition on the core should thus be one of zero tangential field. The application of this boundary condition ensures that the total induced current in the channel is equal and opposite to the excitation current. We choose nondimensional units such that the radius of the limiting torus $a = 1$, and let the tori defined by $\mu = \mu_1$ and $\mu = \mu_2$ represent the channel and core respectively. The channel radius d is then given by

$$d = \operatorname{cosech}\mu_1. \tag{3.4}$$

If we introduce a flux function $\psi(\theta,\mu)$, related to the magnetic field $\boldsymbol{B}$ by $\boldsymbol{B} = \boldsymbol{\nabla}\wedge(0,0,\psi/R)$, where R is the distance from the axis of symmetry, then ψ satisfies

$$\left(\nabla^2-\frac{1}{R^2}\right)\left(\frac{\psi}{R}\right) \equiv \frac{1}{R}\mathrm{D}^2\psi = \mu_0 j_0 \tag{3.5}$$

in $\mu_2 < \mu < \mu_1$, where j_0 is the current distribution of the induction coil, subject to the boundary conditions

$$\frac{\partial\psi}{\partial\mu}(\theta,\mu_2) = \psi(\theta,\mu_1) = 0. \tag{3.6}$$

We solve this problem by means of an expansion in toroidal harmonics.

The general axisymmetric solution of Laplace's equation $\nabla^2 \Phi = 0$ may be expanded as

$$\Phi = H \sum_{n=0}^{\infty} (A_n P^0_{n-\frac{1}{2}}(\cosh\mu) + B_n Q^0_{n-\frac{1}{2}}(\cosh\mu))\, \mathrm{e}^{\mathrm{i}n\theta}, \tag{3.7}$$

where $P^0_{n-\frac{1}{2}}$ and $Q^0_{n-\frac{1}{2}}$ are Legendre functions of the first and second kinds respectively (Morse & Feshbach 1953). The corresponding result for Stokes' equation $\mathrm{D}^2\psi = 0$ is

$$\psi = \frac{\sinh\mu}{H} \sum_{n=0}^{\infty} (A_n P^1_{n-\frac{1}{2}}(\cosh\mu) + B_n Q^1_{n-\frac{1}{2}}(\cosh\mu))\, \mathrm{e}^{\mathrm{i}n\theta}, \tag{3.8}$$

where $P^1_{n-\frac{1}{2}}$ and $Q^1_{n-\frac{1}{2}}$ are associated Legendre functions of the first degree. They may be related to complete elliptic integrals. The P-functions are regular at $\mu = 0$ (the axis of symmetry), but singular at $\mu = \infty$ (the circle $R = 1$, $z = 0$); whereas the Q-functions are singular at $\mu = 0$, but regular at $\mu = \infty$.

The free-space solution ψ_0 for an arbitrary current distribution $j_0(\theta', \mu')$ may be found by a Green-function method. For simplicity we assume that j_0 is symmetric about $\theta = 0$; that is, that the channel is aligned with the centre of the coil. We obtain

$$\psi_0 = \frac{\mu_0}{2\pi}\frac{\sinh\mu}{H} \sum_{n=0}^{\infty} \cos n\theta\, \psi_{0n}(\mu), \tag{3.9}$$

$$\psi_{0n} = \frac{\epsilon_n}{n^2 - \frac{1}{4}} \int_{-\pi}^{\pi} \mathrm{d}\theta' \int_0^{\infty} \mathrm{d}\mu' \frac{\cos n\theta' \sinh\mu'}{H^5(\theta', \mu')} j_0(\theta', \mu')\, W_n(\mu, \mu'), \tag{3.10}$$

where

$$W_n(\mu, \mu') = \begin{cases} P^1_{n-\frac{1}{2}}(\cosh\mu)\, Q^1_{n-\frac{1}{2}}(\cosh\mu') & (\mu < \mu'), \\ Q^1_{n-\frac{1}{2}}(\cosh\mu)\, P^1_{n-\frac{1}{2}}(\cosh\mu') & (\mu > \mu'), \end{cases} \tag{3.11}$$

and $\epsilon_n = 1$ if $n = 0$, $\epsilon_n = 2$ otherwise. The solution to the problem with the boundaries at $\mu = \mu_1$, μ_2 can then be written

$$\psi = \frac{1}{H} \sum_{n=0}^{\infty} \cos n\theta\, F_n(\mu), \tag{3.12}$$

where F_n is of the form

$$F_n = (A_n P^1_{n-\frac{1}{2}}(\cosh\mu) + B_n Q^1_{n-\frac{1}{2}}(\cosh\mu) + \psi_{0n}) \sinh\mu \tag{3.13}$$

for some constants A_n and B_n to be determined from the boundary conditions. The boundary condition at $\mu = \mu_1$ is easy to apply, giving

$$A_n P^1_{n-\frac{1}{2}}(\cosh\mu_1) + B_n Q^1_{n-\frac{1}{2}}(\cosh\mu_1) + \psi_{0n}(\mu_1) = 0 \tag{3.14}$$

because of the linear independence of the functions $\cos n\theta$. The boundary condition at $\mu = \mu_2$, however, is more troublesome because of the multiplicative function $H(\theta, \mu)$ in (3.12). We obtain

$$\sum_{n=0}^{\infty} \cos n\theta\, [(\cosh\mu_2 - \cos\theta)\, F'_n(\mu_2) - \tfrac{1}{2}\sinh\mu_2\, F_n(\mu_2)] = 0 \tag{3.15}$$

or

$$2\cosh\mu_2\, F'_n(\mu_2) - \sinh\mu_2\, F_n(\mu_2) - F'_{n+1}(\mu_2) - F'_{n-1}(\mu_2) = 0. \tag{3.16}$$

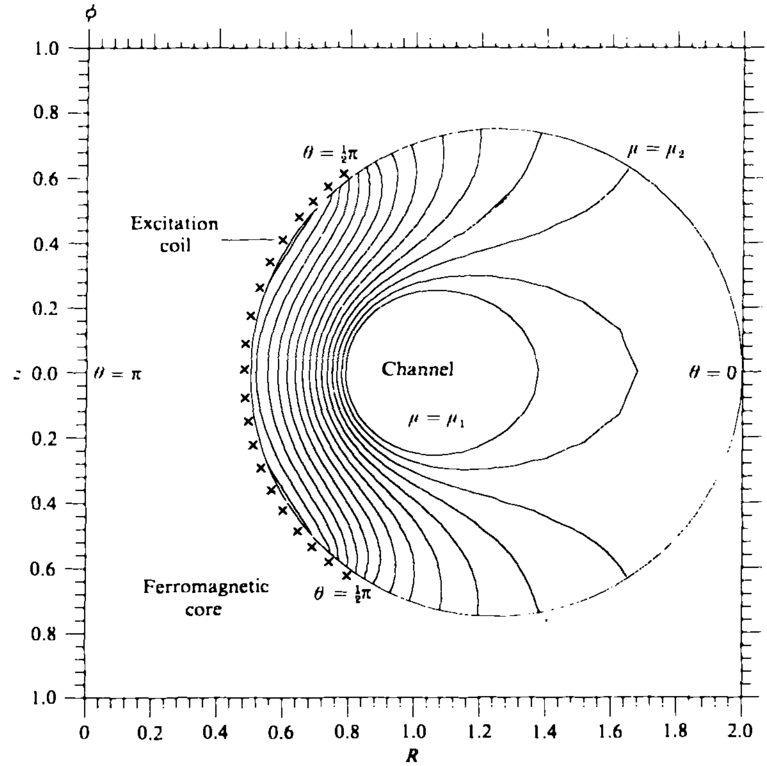

FIGURE 2. Magnetic-field lines for $\delta' = 0$. Core at $\cosh\mu = \frac{5}{3}$; channel at $\cosh\mu = \frac{41}{9}$; excitation coil at $\cosh\mu = \frac{5}{3}$, $\pi > |\theta| > \frac{1}{2}\pi$. Total current = 0.695.

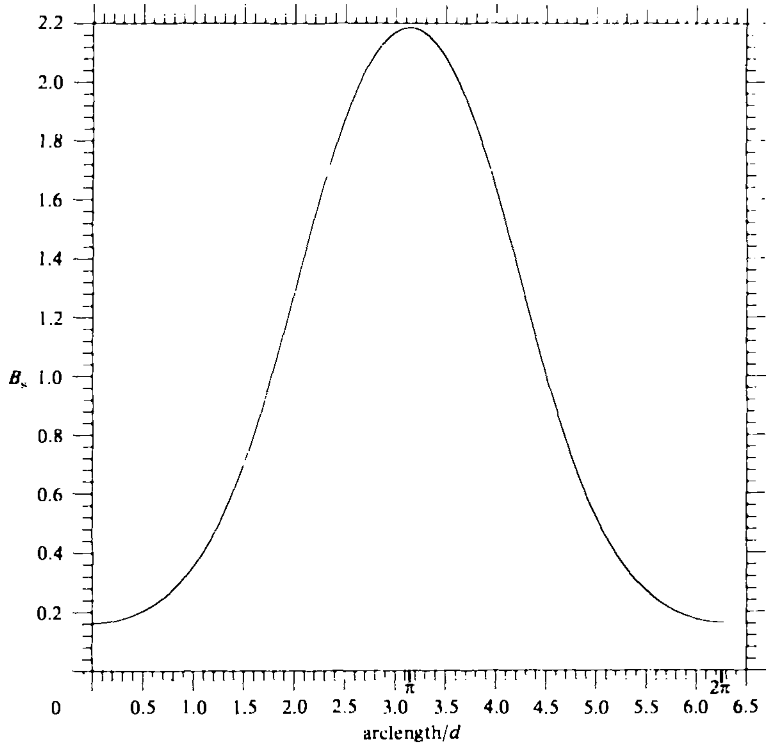

FIGURE 3. Surface field around the channel.

Equations (3.13), (3.14) and (3.16) can be seen to imply

$$\sum_{n=0}^{\infty} M_{mn} A_n = L_m, \tag{3.17}$$

where the infinite square matrix $\boldsymbol{M}$ and vector $\boldsymbol{L}$ may be calculated in terms of j_0, μ_1 and μ_2. The matrix $\boldsymbol{M}$ is tridiagonal; that is, $M_{mn} = 0$ if $|m-n| > 1$. All that remains is to invert this sparse matrix. The numerical methods used to evaluate the field are described in §5.

A typical field pattern is shown in figure 2. The excitation coil has been modelled by a uniform distribution of current along the iron core from $\pi > |\theta| > \frac{1}{2}\pi$. The positions of the core and the channel are marked on the figure, their aspect ratios being $1.\dot{6}$ and $4.\dot{5}$ respectively. The field lines are drawn for the case of zero skin depth, when they are tangential to the channel. The tangential surface field B_s is plotted in figure 3 against arclength around the channel. The heavy field concentration at the inside of the channel is pronounced.

4. The primary fluid motions

The magnetic field inside the metal gives rise to a rotational Lorentz force $\boldsymbol{j} \wedge \boldsymbol{B}$, which drives fluid motions. The force has a steady component, and one oscillating with twice the applied frequency. However, the fluid inertia prevents it from responding to fluctuations on a sufficiently small timescale, and the dominant part of the motion is thus time-independent, and driven by $\boldsymbol{F}$, the mean Lorentz force per unit mass (Mestel 1982). Following Sneyd (1979), we may calculate $\boldsymbol{F}$ and $\boldsymbol{G} \equiv \operatorname{curl} \boldsymbol{F}$ directly from (3.2), giving

$$\boldsymbol{F} = \frac{B_s^2}{2\mu_0 \rho} \frac{1}{\delta'} e^{n/\delta'} (0, 1, 0) \tag{4.1}$$

and

$$\boldsymbol{G} = \frac{H^2}{\mu_0 \rho a} B_s \frac{dB_s}{d\theta} \frac{1}{\delta'} e^{n/\delta'} (0, 0, 1) \equiv (0, 0, G), \tag{4.2}$$

where ρ is the fluid density. A factor of $\frac{1}{2}$ appears in (4.1) and (4.2) because B_s is a r.m.s. value. In some sense G is more important than $\boldsymbol{F}$ in that it represents that part of the forcing that cannot be balanced by a pressure gradient, and so generates rotational motion.

The steady velocity field $\boldsymbol{u}(\theta, \mu)$ is poloidal and satisfies the Navier–Stokes equations

$$\nabla \cdot \boldsymbol{u} = 0, \tag{4.3}$$

$$\boldsymbol{u} \cdot \nabla \boldsymbol{u} = -\nabla \left(\frac{p}{\rho}\right) + \boldsymbol{F} + \nu \nabla^2 \boldsymbol{u}, \tag{4.4}$$

where ν is the kinematic viscosity modified by turbulence, and p is the modified fluid pressure. If we non-dimensionalize distances with respect to the channel width, the magnetic field with respect to a typical value B_0, and velocities with respect to the Alfvén velocity scale

$$V_0 = \left(\frac{B_0^2}{\mu_0 \rho}\right)^{\frac{1}{2}}, \tag{4.5}$$

we obtain for the corresponding vorticity equation ($\boldsymbol{\omega} = \nabla \wedge \boldsymbol{u}$)

$$\nabla \wedge (\boldsymbol{u} \wedge \boldsymbol{\omega}) + \boldsymbol{G} + R_e^{-1} \nabla^2 \boldsymbol{\omega} = 0, \tag{4.6}$$

where

$$\delta = \frac{\delta'}{d}, \quad R_e = \frac{V_0 d}{\nu}. \tag{4.7}$$

Equation (4.6) only has an azimuthal component

$$R\boldsymbol{u}\cdot\nabla\left(\frac{\omega}{R}\right) + G + R_e^{-1}\frac{1}{R}\mathrm{D}^2(\omega R) = 0. \tag{4.8}$$

Now G vanishes outside the magnetic skin layer. Further, even with the effective eddy viscosity, the Reynolds number will be quite large, and so we would expect that viscous forces will only be important near the boundary of the fluid. That being the case, the interior of the flow will be dominated only by inertia forces, with the result that ω/R, the so-called 'potential vorticity', will be constant along streamlines. This is a well-known result for axisymmetric, high-Reynolds-number flows with closed streamlines. An additional result that is of interest was proved by Batchelor (1956). If there exists a closed streamline that never passes through a region where rotational forces act, then inside it the potential vorticity must be constant. This property is illustrated by the numerical calculations below.

The typical velocity scale U_0, and hence the Reynolds number of the flow, is an unknown function of the parameters δ and R_e. If we consider the rate of energy dissipation, from (4.4) we obtain

$$\int \boldsymbol{u}\cdot\boldsymbol{F}\,\mathrm{d}V = \nu\int\frac{\partial u_i}{\partial x_j}\frac{\partial u_i}{\partial x_j}\,\mathrm{d}V. \tag{4.9}$$

The energy dissipation occurs mainly in the boundary layer on the channel wall. Since $\boldsymbol{F}$ is normal to the surface, order-of-magnitude estimates for the terms in (4.9) suggest the balance

$$U_0\,\delta\frac{V_0^2}{\delta}ad\delta = \nu\frac{U_0^2}{L^2}Lad, \tag{4.10}$$

where L is the smallest scale of variation in the boundary layer. When the skin depth δ is smaller than the thickness of the viscous boundary layer, we obtain

$$U_0 = V_0^2\,\delta^2\frac{d}{\nu} = V_0\,R_e\,\delta^2 \tag{4.11}$$

(Moffatt 1982). When the converse occurs, as is certainly the case in an operational channel furnace, we get

$$V_0^2\,\delta = \frac{U_0\,\nu}{d}\left(\frac{U_0\,d}{\nu}\right)^{\frac{1}{2}} \tag{4.12}$$

or

$$U_0 = V_0\,R_e^{\frac{1}{3}}\,\delta^{\frac{2}{3}}. \tag{4.13}$$

The asymptotic relation (4.13) was suggested by some approximate results of Fautrelle (1981, 1983) for a related problem. The two limiting cases, (4.11) and (4.13), appear in the numerical calculations below.

5. Numerical solutions

Solutions have been obtained for various channel sizes, coil geometries and values of R_e and θ. They are all qualitatively similar, and figure 4 portrays a typical flow corresponding to the field distribution of figure 2 when $R_e = 400$ and $\delta = 0.2$. A cross-section of the channel is shown, on which two separate contour plots are drawn.

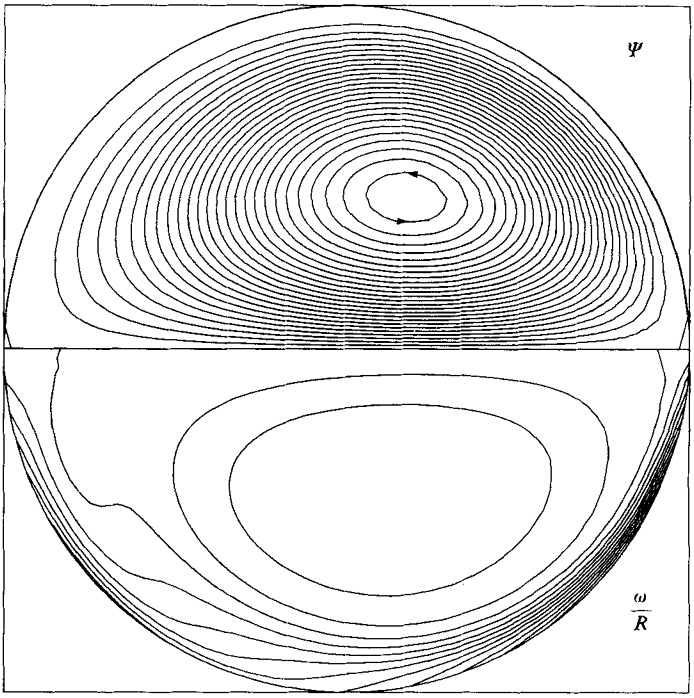

FIGURE 4. Flow pattern for $R_e = 400$, $\delta = 0.2$: streamlines (top) and potential vorticity (bottom).

The streamlines of the flow are plotted on the top half of the figure, and may be compared with the contours of potential vorticity ω/R, which are drawn underneath.

Characteristic of all the flow patterns is a central jet away from the region of maximum magnetic pressure on the left-hand side of the diagram, which recirculates as the far wall is approached. A short distance away from the wall, the velocity is large and comparable to the speed of the jet, but it falls away rapidly across the boundary layer in order to comply with the no-slip condition. This strong shear is clearly visible in the potential-vorticity plots. Throughout most of the fluid the vorticity is negative, but in the boundary layer it becomes strongly positive. Other features of the flow vary as the parameters R_e and δ change. For relatively small Reynolds number, the centre of the circulation lies close to the left-hand side of the diagram where the forcing G is largest. As R_e is increased, however, the inertia forces become more important and the flow appears to approach its pure 'inertial' limit of constant ω/R, for which the centre is offset slightly to the right. The position of maximum wall stress also moves to the right as the Reynolds number is increased, towards the region where the central jet impinges. It should be remembered, however, that the turbulence model we have used is at its least applicable near the wall, and may not give accurate results for the wall stress.

As the penetration depth δ is decreased with R_e held constant, the velocity magnitude decreases with δ. The gradients of potential vorticity outside the boundary layer lessen as the plateau regions begin to be formed, until the viscous and magnetic boundary layers are of equal thickness. In the very-high-frequency limit (as $\delta \to 0$) it might be possible to make some analytic progress (cf. Moffatt 1982), but this does not correspond to a realistic parameter range for an operational furnace. The

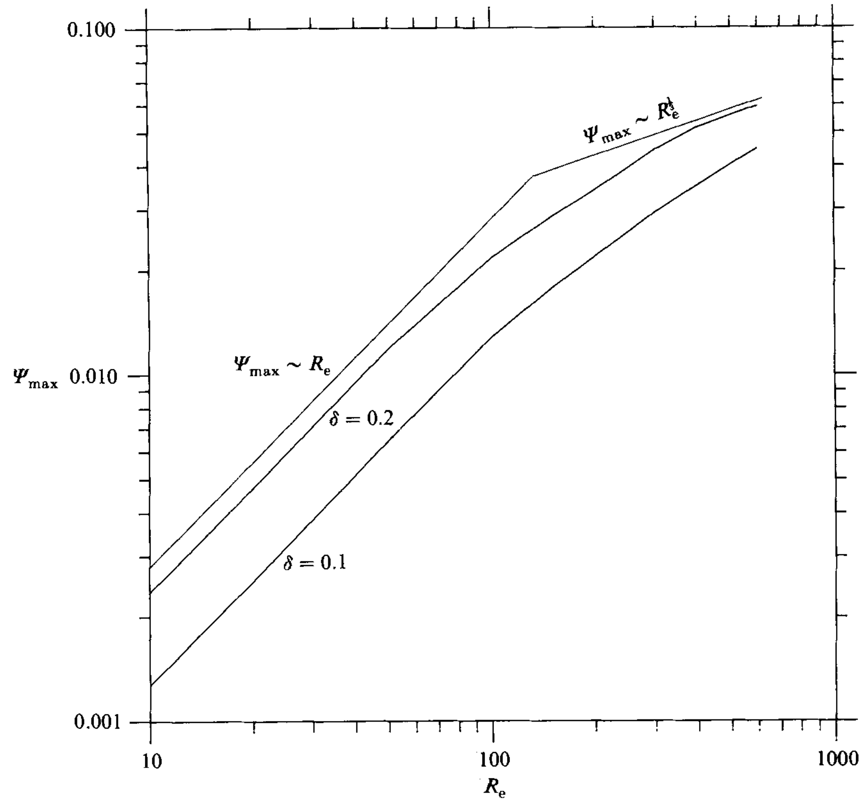

FIGURE 5. Flow strength ($\Psi_{\max}$) as a function of viscosity (R_e) for $\delta = 0.1$, 0.2.

asymptotic result (4.11) is approached more slowly than expected, as we find numerically that the coefficient of δ^3 is larger than that of δ^2.

A measure of the flow velocity U_0 is provided by the maximum absolute value $\Psi_{\max}$ attained by the stream function. This is plotted against R_e on log–log axes in figure 5 for $\delta = 0.1$ and 0.2. The gradients predicted in §4 are indicated on the diagram. For relatively low values of R_e, the relation (4.11) is satisfied very closely. The asymptotic regime for which (4.13) holds has not quite been reached, the computations becoming quite expensive for large Reynolds number.

6. Numerical methods

6.1. *Evaluation of the magnetic field*

Although the solution given in (3.12) is in closed form, it is, of course, necessary to evaluate it on a computer before one obtains any intuitive idea of the behaviour of the field lines. We truncate the series after some large number of terms, N, which we then vary to ensure that adequate convergence has been obtained. For a given value of μ we calculate the values of the associated Legendre functions P and Q by means of the recurrence relation

$$(n-\tfrac{1}{2})\, P^1_{n+\frac{1}{2}} = 2n \cosh\mu\, P^1_{n-\frac{1}{2}} - (n+\tfrac{1}{2})\, P^1_{n-\frac{3}{2}}. \qquad (6.1)$$

The same relation holds for the Q-functions as for the P-functions. The starting values $P^1_{-\frac{1}{2}}$ and $P^1_{\frac{1}{2}}$ may be simply calculated in terms of complete elliptic integrals. The formulae used were taken from Abramowitz & Stegun (1965), although a confusing notational inconsistency was discovered between the relevant chapters. The P-values for higher n may be calculated accurately by straightforward application of (6.1). The same process fails, however, if used for the Q-functions. This is because the P-functions increase rapidly with n, and thus a small error in evaluating the early Q-functions, which is reflected in a small coefficient of a P, soon becomes magnified and completely swamps the real solution. Fortunately, a simple alternative method is available. If we choose arbitrary values for the Qs for large consecutive values of $n \gg N$, (6.1) may be used to iterate backwards towards $n = 0$. The exact value of $Q^1_{-\frac{1}{2}}$ is found from an elliptic-integral formula, and this value is used to normalize the entire set of Q-values. The new values are very accurate except near the very end, for the same reason that the other method fails. A small error for low values of n would give rise to a massive error for large n, whereas the error for large n has been constrained by our initial arbitrary choice.

As well as the P- and Q-values, which we can now find, we require their derivatives with respect to μ. These are best found from the relation

$$\sinh\mu \frac{\mathrm{d}}{\mathrm{d}\mu} P^1_{n-\frac{1}{2}} = (n-\tfrac{1}{2}) \cosh\mu\, P^1_{n-\frac{1}{2}} - (n+\tfrac{1}{2})\, P^1_{n-\frac{3}{2}} \tag{6.2}$$

and a similar one for Q.

The first N terms in the expansion of ψ_0 we calculate by numerical integration, for a given choice of current distribution j_0. We may then calculate the values of M and L. To solve the truncated equation (3.17) we use a NAG inversion routine. The field lines may then be plotted by contouring ψ, as given by (3.12). The surface field B_s may be evaluated, and it is a useful check then to integrate it around the channel, which gives one the total induced current. This may then be compared with the total excitation current, to which it should be equal and opposite.

6.2. *The Navier–Stokes equations*

We aim to solve (4.6) by a finite-difference method. If we define a stream function Ψ by $\boldsymbol{u} = \boldsymbol{\nabla} \wedge (0, 0, \Psi/R)$, and introduce time dependence to the problem, the equations to be solved are

$$\frac{\partial \omega}{\partial t} = H^4 \frac{\partial(\Psi, \omega/R)}{\partial(\mu, \theta)} + G + \frac{R_e^{-1}}{R} D^2(\omega R), \tag{6.3}$$

where the second term is a Jacobian, and

$$-\omega R = \mathrm{D}^2 \Psi \tag{6.4}$$

in $\mu_1 < \mu < \infty$, $0 < \theta < \pi$ with boundary conditions

$$\Psi(\theta, \mu_1) = \Psi(0, \mu) = \Psi(\pi, \mu) = \Psi(\infty, \theta) = 0 \tag{6.5}$$

and

$$\frac{\partial}{\partial \mu} \Psi(\theta, \mu_1) = \frac{\partial \Psi}{\partial \theta}(0, \mu) = \frac{\partial \Psi}{\partial \theta}(\pi, \mu) = 0. \tag{6.6}$$

In order to regularize the behaviour about $\mu = \infty$, we rescale the μ-coordinate by writing

$$(1 - \tanh\mu_1)\, s^2 = 1 - \tanh\mu \tag{6.7}$$

and define a uniform grid in s and θ. Derivatives are then approximated by second-order difference relations, and the equations are time-stepped towards equilibrium using the method described by Mestel (1982).

7. Non-axisymmetric perturbations

Having found the primary flow, we are now in a position to consider the effects of small variations of the system from axisymmetry. The return path of the iron core has a very weak effect on the field distribution, because it has relevance only in the region where the field is small, on the far side of the channel from the excitation currents. Of far greater importance is the presence of the bath above the channel. This we shall model by assuming the channel shape to be given by

$$\mu = \mu_1 - \epsilon f(\theta, \phi), \tag{7.1}$$

where ϵ is a suitably small parameter. A glance at figure 1 (*c*) reveals that the function f will be localized about $\phi = 0$ on the scale of the angle subtended at the centre of the torus by the junctions of channel and bath. Further, f should be much greater at $\theta = 0$ (the top of the bath) than at $\theta = \pi$ (the bottom).

The magnetic field outside the channel now takes the form

$$\boldsymbol{B} = \boldsymbol{B}_0 + \epsilon \nabla V, \tag{7.2}$$

where V satisfies Laplace's equation. For $\boldsymbol{B}$ to be normal to the core and tangential to the channel we require

$$V(\mu_2) = 0, \quad \frac{\partial V}{\partial \mu}(\mu_1) = -H^4 \frac{\partial}{\partial \theta}\left(\frac{B_s f}{H^4}\right). \tag{7.3}$$

If we assume for simplicity that the shape perturbation $f(\theta, \phi)$ maintains the symmetry about $\theta = 0$, then V may be expanded

$$V = H \sum_{n=0}^{\infty} \sum_{m=0}^{\infty} \sin n\theta \, \mathrm{e}^{\mathrm{i}m\phi} \left[C_{nm} P^m_{n-\frac{1}{2}}(\cosh \mu) + D_{nm} Q^m_{n-\frac{1}{2}}(\cosh \mu)\right]. \tag{7.4}$$

Application of the boundary conditions (7.3) then yields for each harmonic number m an equation for the coefficients C_{nm} of the form (3.17). These we solve numerically as before. We may now calculate the perturbed Lorentz force

$$F = \left(\tfrac{1}{2}B_s^2 + \epsilon H^2 B_s \frac{\partial V}{\partial \theta}\right) \frac{1}{\mu_0 \rho \delta} \mathrm{e}^{n/\delta} \left(\epsilon H^2 \frac{\partial f}{\partial \theta}, 1, \frac{\epsilon}{R}\frac{\partial f}{\partial \phi}\right) + O(\epsilon^2), \tag{7.5}$$

and, in principle, could continue to solve the linearized Navier–Stokes equations for each m to find the perturbed velocity field. This somewhat lengthy calculation has not been done, and we confine ourselves here to some general remarks on the form of the secondary flow.

The driving force of (7.5) varies significantly in the azimuthal direction only in the region at the top where the channel joins the bath. Thus, apart from a possible bulk motion along the channel, we would expect it to drive a circulatory cell of a lengthscale similar to that of the channel top. This cell will then drive a series of successively weakening cells down the sides of the channel, whose influence will be least at the bottom. However, heat is being generated by Joule dissipation uniformly along the channel, and must be convected into the bath, where it is lost to the surroundings. Thus, if the net drift along the channel is small, the weak convection at the bottom of the channel may very well lead to large temperature differences between the top and the bottom. These are undesirable, as resultant surges of buoyant fluid may hasten the wear on the refractory lining, quite apart from efficiency considerations. A healthy mean circulation is therefore a prime consideration in furnace design.

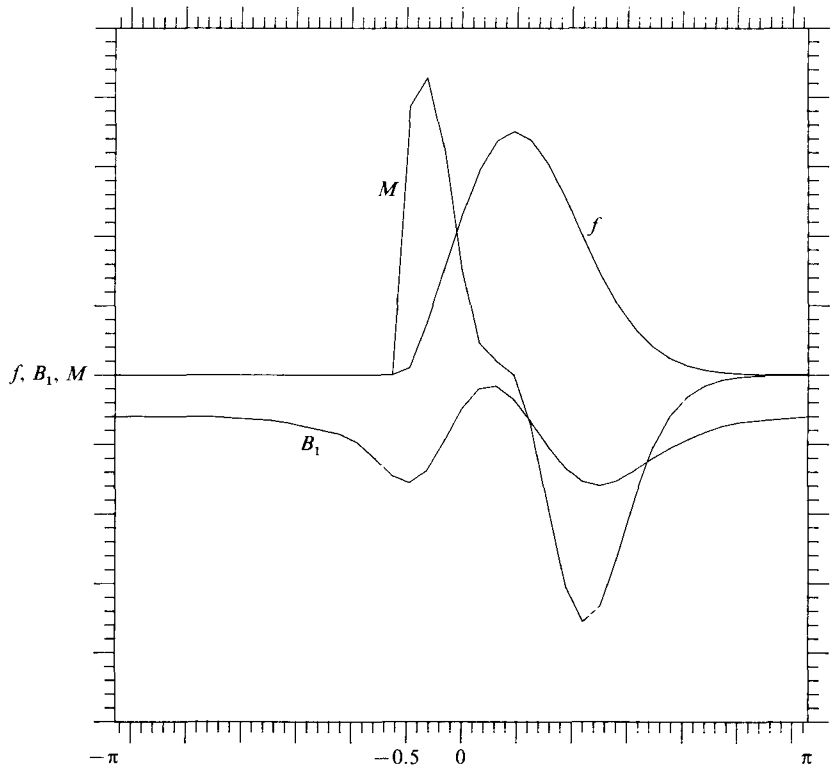

FIGURE 6. Perturbation functions f, B_1 and M at $\theta = \pi$.

Returning to the model, however, we notice that to order ϵ there is no mean circulation along the channel, because the azimuthal driving force has a total moment M^* about the axis of symmetry, given by

$$M^* = 2\epsilon^2 \int_0^\pi \frac{\mathrm{d}\theta}{H^2(\mu_1, \theta)} \int_{-\pi}^{\pi} R \,\mathrm{d}\phi\, M(\theta, \phi) + O(\epsilon^3), \tag{7.6}$$

where

$$M = B_s \frac{\partial f}{\partial \phi} B_1(\theta, \phi), \quad B_1 = H^2(\mu_1, \theta) \frac{\partial V}{\partial \theta}, \tag{7.7}$$

which is of second order. The net drift must therefore be found from the second-order equation for $m = 0$. Now M^* will vanish if the perturbation f is an even function of ϕ, that is, if the entrance and exit regions of the channel into the bath are symmetric. In practice, it clearly pays to introduce some asymmetry if a circulation is desired. Ideally, we would wish to calculate the size and direction of the mean circulation for any particular furnace design. We might attempt to model the effect of a sharp corner on one end of the channel and a rounded one on the other by means of the perturbation

$$f = \frac{(\phi + 0.5)\,\mathrm{e}^{-\phi^2}}{1 + \theta^2 + \phi^2} \quad (\pi > \phi > -0.5), \quad f = 0 \quad (-\pi < \phi < -0.5) \tag{7.8}$$

for $\pi > \theta > -\pi$. For this function, and the basic field of figure 2, we calculate the surface-field perturbation $B_1(\theta, \phi)$. In figure 6, with suitable scalings, we plot f, B_1 and M as functions of ϕ evaluated along the inner part of the channel ($\theta = \pi$). The field perturbation B_1 is negative because the increase in channel surface area leads to a decrease in the surface current. The moment M depends on the direction of the normal, that is, on the gradient of f. It is discontinuous at the sharp corner $\phi = -0.5$. For this case we find that the total moment $M^* < 0$. It should be noted, however, that the sign of M^* does not necessarily give us the direction of circulation. If we take the moment of (4.4) about the axis of symmetry, integrate about the unperturbed torus and ignore the viscous term, we get

$$\frac{\partial}{\partial t}\int_{\mu>\mu_1} Ru_\phi \, \mathrm{d}V = M^* - \int_{\mu=\mu_1} Ru_\phi u_\mu \, \mathrm{d}S. \tag{7.9}$$

We see that it is possible for the angular-momentum flux from the first-order flow to be such as to generate a mean circulation in the opposite sense to M^*. Once the first-order flow has been evaluated, however, this circulation may be calculated.

8. Concluding remarks

The axisymmetric cross-sectional primary flow holds no great surprises for us, the fluid reacting to the highly localized driving force in a predictable manner. Of greater interest and complexity are the secondary motions, into which the perturbation approach we have described in §7 may give some insight. The perturbation approximation is valid provided that the influence of the bath region remains small, which is probably the case as far as the magnetic field is concerned. It is, however, questionable whether the nonlinear dynamical effects of the bath and its distant boundaries can be more than qualitatively modelled by means of a shape perturbation. Should the induced bath flow be approximately symmetric with respect to the entrance and exit regions of the channel, however, it seems likely that the perturbation method will give a good estimate for the *mean* circulation along the channel, as the effects of nonlinearity in the bath should cancel. This may be expected to occur when the bath walls are of regular shape and symmetrically placed, so that the only asymmetry occurs in the channel regions. An order of magnitude for the circulation rate would then be $\epsilon^2 U_0$.

Our use of the no-slip boundary condition at the top of the channel has formally neglected any possible effect of a free surface in the bath. However, the model will still apply, provided that the fluid motions at the top of the bath are weaker than those at the bottom. This will presumably occur if the depth of fluid in the bath is large compared with the channel size, as is the case in practice.

We have assumed throughout this paper that the 'eddy viscosity' ν is known. In practice, of course, it must be supplied by experimental measurement. We might expect it to be proportional to the velocity magnitude and the channel width, so that

$$\nu \sim V_0 \Psi_{\max} d. \tag{8.1}$$

This somewhat simplistic reasoning would predict that observations of the velocity scale U_0 would obey

$$U_0 \sim V_0 \delta \tag{8.2}$$

as the channel dimensions (and hence δ) are varied. A more detailed discussion of the effects of turbulence in this sort of flow may be found in Hunt & Maxey (1980).

The author is grateful to Drs Hunt, Proctor and Lillicrap for several interesting and informative discussions. The work was stimulated and partially supported by the Electricity Council Research Centre at Capenhurst.

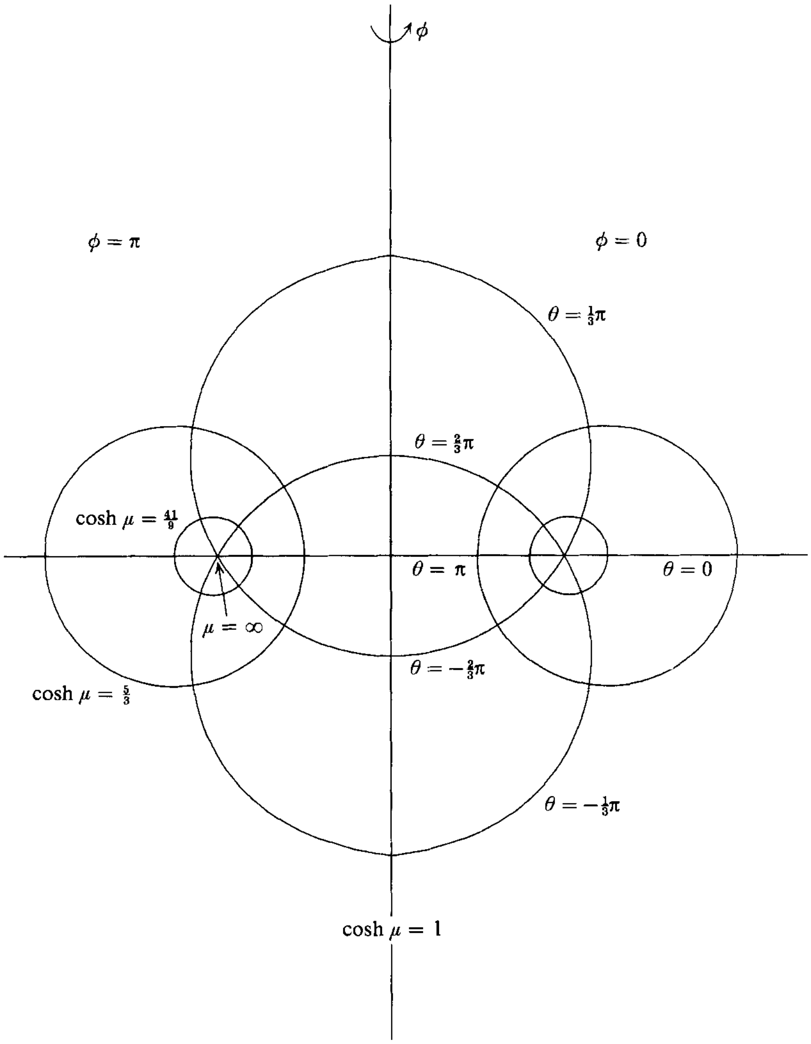

Appendix. Toroidal coordinates

The toroidal coordinate system is obtained by rotating bipolar coordinates about their axis of symmetry. Bipolar coordinates are defined by a family of circles passing through two fixed points. The orthogonal set of curves are coaxial circles whose axis is the perpendicular bisector of the line joining the two points. Upon rotation about the axis, the coordinate curves become coordinate surfaces, which are respectively spheres passing through a given circle, and a set of tori surrounding that circle. The third set of orthogonal surfaces are the axial planes, corresponding to constant azimuthal angle ϕ.

We arrange the z-axis of a Cartesian system to lie along the ϕ-axis, and define the fixed circle by $x^2+y^2 = a^2$, for some constant a. We may now define coordinates $-\pi < \theta < \pi$ and $0 < \mu < \infty$, such that the spheres have radius $a/|\sin\theta|$ and centre

$(0, 0, a\cot\theta)$, while the tori have inner radius $a/\sinh\mu$ and outer radius $a\coth\mu$. The aspect ratio of the torus is thus measured by $\cosh\mu$. With these coordinates,

$$x = \frac{a\sinh\mu\cos\phi}{\cosh\mu-\cos\theta}, \quad y = \frac{a\sinh\mu\sin\phi}{\cosh\mu-\cos\theta}, \quad z = \frac{a\sin\theta}{\cosh\mu-\cos\theta}.$$

The scale factors are given by

$$h_\theta = h_\mu = \frac{a}{\cosh\mu-\cos\theta}, \quad h_\phi = R = \frac{a\sinh\mu}{\cosh\mu-\cos\theta}.$$

Some coordinate lines are sketched in figure 7. A fuller description of toroidal coordinates may be found in Morse & Feshbach (1953).

REFERENCES

ABRAMOWITZ, M. & STEGUN, I. A. 1965 *Handbook of Mathematical Functions*. Dover.

ALDEN, R. T. H., BURKE, P. E. & BIRINGER, P. P. 1970 MHD pumping in channel furnaces. In *Proc. IEEE Winter Power Meeting, New York, 1970. IEEE Conf. Paper.*

BATCHELOR, G. K. 1956 On steady laminar flow with closed streamlines at large Reynolds number. *J. Fluid Mech.* **1**, 177.

FAUTRELLE, Y. R. 1981 Analytical and numerical aspects of the electromagnetic stirring induced by alternating magnetic fields. *J. Fluid Mech.* **102**, 405.

FAUTRELLE, Y. R. 1983 Single phase electromagnetic stirring in coreless induction furnaces. *Liquid Metal Flows and Magnetohydrodynamics*, p. 374. AIAA Prog. Astro. Aero.

HUNT, J. C. R. & MAXEY, M. R. 1980 Turbulent flows of liquid metals. In *MHD-Flows and Turbulence II* (ed. H. Branover & A. Yakhot), p. 249. Israel Universities Press.

MESTEL, A. J. 1982 Magnetic levitation of liquid metals. *J. Fluid Mech.* **117**, 27.

MOFFATT, H. K. 1982 High frequency excitation of liquid metal systems. In *Proc. IUTAM Symp. on Metallurgical MHD, Cambridge, 1982* (in press).

MORSE, P. M. & FESHBACH, H. 1953 *Methods of Theoretical Physics*. McGraw-Hill.

SCHLUCKEBIER, D. 1973 Inductors – particularly high power units – for melting heavy metal. In *Proc. 5th Intl Junker Furnace Conf., Lammersdorf, 1973*, p. 188; *Electrowärme Intl* **31** (1973) B6, 270.

SNEYD, A. D. 1979 Fluid flow induced by a rapidly alternating or rotating field. *J. Fluid Mech.* **92**, 35.